Non-intrusive Characterization of the Wear of the HERMeS Thruster Using Optical Emission Spectroscopy

IEPC-2019-841

Presented at the 36th International Electric Propulsion Conference
University of Vienna, Austria
September 15-20, 2019

Timothy G. Gray*, George J. Williams, Jr.†, Hani Kamhawi‡, and Jason D. Frieman§
NASA Glenn Research Center, Cleveland, OH, 44135, USA
and
Ioannis Mikellides¶
Jet Propulsion Laboratory, California Institute of Technology, Pasadena, CA, 91109, USA

The Hall Effect Rocket with Magnetic Shielding (HERMeS) is a 12.5 kW Hall thruster electric propulsion string that has been in development by NASA Glenn Research Center (GRC) and NASA JPL since 2012. Due to the magnetically shielded design, service life-limiting erosion of the boron nitride discharge has been virtually eliminated. The inner front pole cover has now been identified as the component defining erosion-based service life. Optical emission spectroscopy (OES) is used as an in-situ diagnostic to measure relative erosion trends during operation of the HERMeS thruster during a series of short duration wear tests. Erosion trends obtained from the OES data is compared to traditional erosion data measured with a non-contact profilometer.

Nomenclature

a_0	= Bohr radius
B	= thruster magnetic field
C_{crm}	= CRM correction factor
E_i, E_j	= energy of ith and jth electronic states
f_{ij}	= absorption oscillator strength of the $i \rightarrow j$ optical transition
g_i, g_j	= statistical weight (multiplicity) of ith and jth states
I	= intensity of emission line
i, j	= quantum numbers of the initial and final states
k	= Boltzmann constant
k_{ij}	= rate coefficient for transition from i to j
m_e	= electron mass
n_0	= density of ground state
n_e	= electron density
n_i, n_j	= density of ith and jth excited states
Ry	= Rydberg energy
T_e	= electron temperature

*Research AST, Electric Propulsion Systems Branch, timothy.g.gray@nasa.gov.
†Research AST, Electric Propulsion Systems Branch, george.j.williams@nasa.gov.
‡Ion Propulsion System Test Lead, Electric Propulsion Systems Branch, hani.kamhawi-1@nasa.gov.
§Research AST, Electric Propulsion Systems Branch, jason.d.frieman@nasa.gov.
¶Principal Engineer, Electric Propulsion Group, Ioannis.g.Mikellides@jpl.nasa.gov.

I. Introduction

NASA continues to evolve a human exploration approach for beyond low-Earth orbit and to do so, where practical, in a manner involving international, academic, and industrial partners.[1] Towards that end, NASA publicly presented a reference exploration concept at the Human Exploration and Operations Mission Directorate (HEOMD) Committee of the NASA Advisory Council meeting on March 28, 2017.[2] This approach is based on an evolutionary human exploration architecture, expanding into the solar system with cislunar flight-testing and validation of exploration capabilities followed by crewed missions.

The center of this approach is NASA's Gateway that is envisioned to provide a maneuverable outpost in Lunar orbit to extend human presence in deep space and expand on NASA exploration goals. The Gateway represents the initial step in NASA's architecture for human cislunar operations, lunar surface access, and missions to Mars. NASA recently announced plans to send astronauts to the Lunar surface by 2024 as part of the newly formed Artemis program. A key enabling aspect of the Artemis program is the Gateway that provides access to the Moon surface. The first element of the Gateway is the Power and Propulsion Element (PPE), illustrated in Fig. 1, in which NASA recently announced a commercial partnership to develop and demonstration a high-powered Solar Electric Propulsion (SEP) spacecraft with Maxar Technologies, formerly SSL.[3] The PPE will reach and maintain Lunar orbit by incorporating two high-powered SEP systems developed by NASA, in partnership with Aerojet Rocketdyne, and Maxar.[4] The PPE is baselined to include two 13-kW Advanced Electric Propulsion System (AEPS) thrusters and four 6-kW Hall thrusters, currently under development by Maxar, for a total beginning of life propulsion power of over 60 kW.[4]

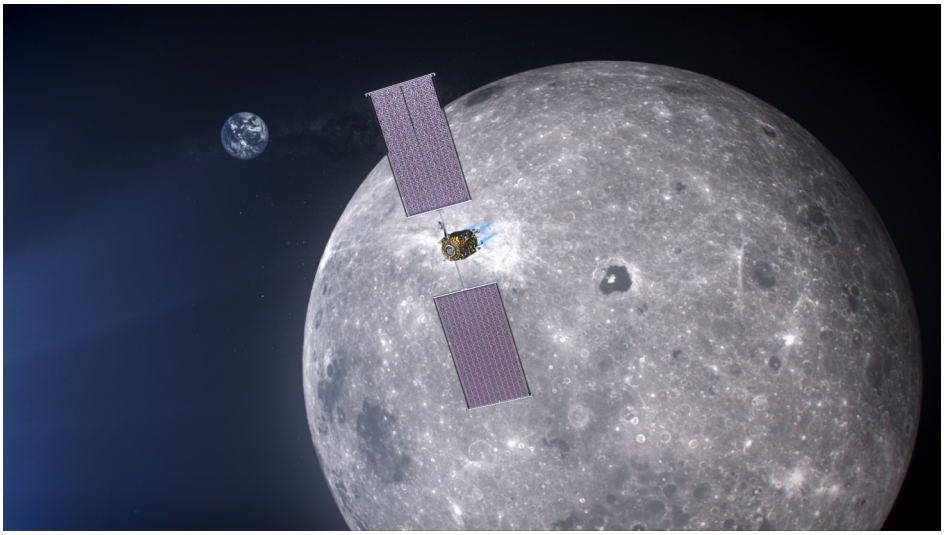

Figure 1: NASA concept of the Power Propulsion Element (PPE) [Credits: NASA].

High-power solar electric propulsion is one of the key technologies that has been prioritized because of its significant exploration benefits, specifically, for missions beyond low Earth orbit. Spacecraft size and mass are dominated by onboard chemical propulsion systems and propellants that may constitute more than 50 percent of spacecraft mass. This impact can be substantially reduced through the utilization of SEP, due to its higher specific impulse and lower propellant load required to meet the equivalent mission delta-V. Studies performed for NASA's HEOMD and Science Mission Directorate (SMD) have demonstrated that a 40-kW-class SEP provides the necessary capabilities that would enable near term and future architectures, and science missions.[5]

Accordingly, since 2012, NASA has been developing a 13-kW-class Hall thruster electric propulsion string that can serve as the building block for a 40-kW-class SEP capability. The 13-kW Hall thruster electric propulsion string development, led by the NASA Glenn Research Center (GRC) and the Jet Propulsion Laboratory (JPL), began with maturation of the high-power Hall thruster and Power Processing Unit (PPU). The technology development work has transitioned to Aerojet Rocketdyne via a competitive procurement selection for the AEPS contract in May, 2016. The AEPS Electric Propulsion (EP) string consists of the Hall Current Thruster (HCT), PPU (including digital control and interface functionality), Xenon Flow Controller

(XFC), and associated intra-string harnesses. Management of the AEPS contract is being led by NASA GRC with funding from NASA's Space Technology Mission Directorate (STMD). NASA continues to support the AEPS string development leveraging in-house expertise, plasma modeling capability, and world-class test facilities. NASA also executes risk reduction activities to support the AEPS string development and mission application.

During the design phase of the 12.5 kW Hall Effect Rocket with Magnetic Shielding (HERMeS) thruster, the approach was to design a magnetic circuit that leveraged all the lessons learned from the H6MS and the NASA-300MS thruster work.[6,7] The Technology Demonstration Unit (TDU) magnetic field topology was shielded to assure that discharge channel erosion was eliminated. This was validated by a wall probe test that was performed at discharge voltages up to 800 V.[8] The wear tests of the HERMeS TDU-1 and TDU-3 thrusters found that discharge erosion rates were minimized; however, measurable erosion of the front pole covers was found. While the rates were lower than discharge channel erosion rates of unshielded thrusters, front pole cover erosion became the next life-limiting mechanism.[9–12]

Traditionally, measurement of erosion of front pole covers is intrusive and not in-situ, as testing must be interrupted and the thruster must either be partially disassembled or fully removed from the test environment for erosion characterization. Non-intrusive techniques for measuring erosion are desirable, particularly ones that can be deployed to make in-situ measurements of erosion of thruster components in the test environment. Optical emission spectroscopy (OES) is one technique that has been successfully used to measure erosion of the boron nitride discharge channel, and preliminary results have been obtained for inner front pole cover (IFPC) erosion.[13] In addition to being in-situ, the OES technique can obtain real-time, relative erosion rates during thruster operation.[14]

A series of short duration wear tests of the HERMeS thruster were conducted at NASA GRC to characterize performance of several different magnetic configurations. The OES data was collected from the front face of the thruster. The OES data from the thruster face and near-field electron temperatures were synthesized to estimate IFPC erosion. Erosion trends obtained from the OES data will be compared to traditional erosion data measured with a non-contact profilometer.

II. Emission Spectroscopy

The optical emission spectroscopy diagnostic implemented in this investigation used a C I transition with an emission line at 247.9 nm. The intensity of spectral line emission from the radiative decay from bound states $j \rightarrow i$ is given by

$$I_{ji} = N_j A_{ji} \hbar \omega_{ji} \tag{1}$$

where N_j is the total number of atoms in state j, A_{ji} is the Einstein coefficient for spontaneous emission, $\hbar$ is the reduced Planck constant, and ω_{ji} is the transition frequency. Measuring the intensity of emitted light at a line of interest can be used to determine the total number (and number density) of a population of atoms. Carbon sputtered from the inner front pole cover will be excited by the thruster plasma and its total density should be correlated to erosion rates. The total population of carbon atoms will be partitioned amongst the available electronic states in a fashion that is dependent on local electron density and temperature. In order to account for this impact on the upper state population of the transition of interest, a model must be constructed.

A. Collisional-Radiative Model

For a simplified system with only collisional excitation to state j and radiative decay from state j, the density of state j is

$$n_j = n_i n_e k_{ij} \tag{2}$$

where n_i is the neutral density in the lower ith state, n_e is the electron density, and k_{ij} is the excitation rate constant for the transition. The rate constants have a dependence on electron temperature that is not explicitly shown. A system with multiple levels and collisional excitation/deexcitation calls for a more complex model.

Taking an approach similar to Rock,[15] a rudimentary collisional-radiative model (CRM) was constructed for the purposes of correlating the C I emissions at 247.9 nm to sputtered carbon density. The levels represented in the model are illustrated in Fig. 2 and relevant parameters for the bound states are listed in Table 1.[16] The bound states in the model are labeled $i, j = 0$–3, with the ground state being 0, and the

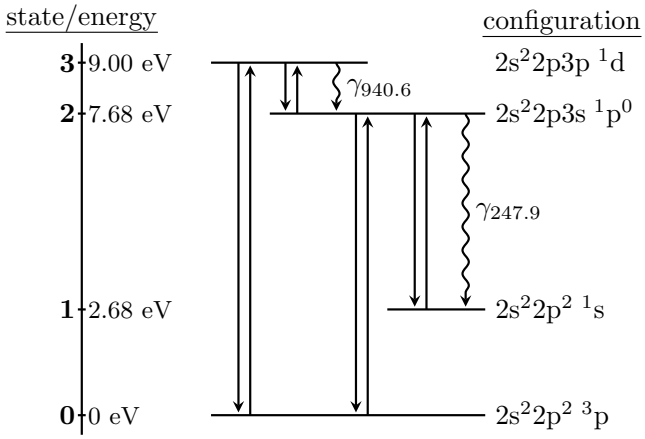

Figure 2: Simplified level diagram for the collisional radiative model. Collisional excitation and deexcitation are represented by solid arrows and radiative decay by wiggly arrows. States referred to in the model are labeled on the left axis.

Table 1: Atomic transition parameters.

species	A_{ji} (s^{-1})	lower state	g_i	E_i (eV)	upper state	g_j	E_j (eV)	λ (nm)
C I	2.80×10^7	$2s^22p^2\ ^1s$	1	2.68	$2s^22p3s\ ^1p^0$	3	7.68	247.9
C I	2.91×10^7	$2s^22p3s\ ^1p^0$	3	7.68	$2s^22p3p\ ^1d$	5	9.00	940.6

label incrementing with increasing energy for a given state. The 247.9 nm transition is to a metastable state with no allowed optical transitions to the ground state. Even though the 940.6 nm line was not diagnosed, it is included in the model because its Einstein coefficient A_{ji} is large and the lower state of the transition is the upper state of the 247.9 nm transition.

The rate equations which determine the rate of change of the population densities for a bound level j can be written as

$$\frac{\mathrm{d}n_j}{\mathrm{d}t} = \sum_i n_e n_i R_{i\to j} \tag{3}$$

where n_j, n_i are the densities of the ith and jth states, n_e is the electron density, and $R_{i\to j}$ represents all rates contributing to the transition $i \to j$. The model being built is a steady state model, so the left hand side of Eq. (3) is set to zero. A set of equations is constructed for each final state in the model; in the case of the CRM used for this work, there are four states, which leads to four equations. This system of equations can be represented in matrix form and solved using linear algebra techniques; singular value decomposition (SVD) techniques were used in the current work.

$$\begin{pmatrix} -R_{0\to0} & R_{1\to0} & R_{2\to0} & R_{3\to0} \\ R_{0\to1} & -R_{1\to1} & R_{2\to1} & R_{3\to1} \\ R_{0\to2} & R_{1\to2} & -R_{2\to2} & R_{3\to2} \\ R_{0\to3} & R_{1\to3} & R_{2\to3} & -R_{3\to3} \end{pmatrix} \begin{pmatrix} n_0 \\ n_1 \\ n_2 \\ n_3 \end{pmatrix} = \begin{pmatrix} 0 \\ 0 \\ 0 \\ 0 \end{pmatrix} \tag{4}$$

Terms with the form $R_{i\to i}$ are depopulation rates, which are equal to the sum over all rates for which state i populates other states, i.e.:

$$R_{0\to0} = R_{0\to1} + R_{0\to2} + R_{0\to3} \tag{5}$$

As an example, the rates for the $2 \to 1$ transition include collisional deexcitation ($n_e k_{21}$) and radiative decay (A_{21}).

$$R_{2\to1} = n_e k_{21} + A_{21} \tag{6}$$

Collisional excitation ($n_e k_{12}$) from $1 \to 2$ is included in the $R_{1\to2}$ rate.

The collisional excitation rate constants k_{ij} can be calculated using the semi-empirical Van Regemorter model presented in Sobel'man[17]

$$k_{ij} = 32 \cdot 10^{-8} f_{ij} \left(\frac{Ry}{\Delta E} \right)^{3/2} \beta_{ij}^{1/2} e^{-\beta_{ij}} \cdot p(\beta_{ij}) \tag{7}$$

where the values of $p(\beta)$ are tabulated in Sobel'man. β_{ij} is a function of the excitation energy ($\Delta E = E_j - E_i$) and the electron temperature (T_e).

$$\beta_{ij} = \frac{E_j - E_i}{kT_e} = \frac{\Delta E}{kT_e}. \tag{8}$$

The rate constants were also calculated using the semi-empirical Drawin model discussed in Chernyi:[18]

$$k_{ij}(T_e) = 8\pi a_0^2 \left(\frac{Ry}{W_{ij}} \right)^2 f_{kn} \cdot \sqrt{\frac{2kT_e}{\pi m_e}} (\beta_{ij}) [\Psi_{ij} + 0.1 e^{-\beta_{ij}}] \tag{9}$$

where

$$\Psi_{ij}(\beta) = \int_{\beta_{ij}}^{\infty} \left(1 - \frac{\beta_{ij}}{t} \right) e^{-t} \cdot \ln \left(1.25 \frac{t}{\beta_{ij}} \right) \mathrm{d}t \,. \tag{10}$$

Model results using these alternate rate constants were not significantly different from those calculated using Eq. (7) and will not be discussed further.

Deexcitation rates were calculated using the principle of detailed balance, from which the relation between excitation and deexcitation rates can be derived.

$$k_{ji} = \frac{g_i}{g_j} k_{ij} e^{\beta_{ji}} \tag{11}$$

where g_i an g_j are the degeneracies of the ith and jth states.[17]

The $R_{i \to j}$ rates in Eq. (4) were thus constructed for each pair of bonded states. Collisional excitation and deexcitation rates were calculated for each pair of states, with the exception of the ground state/metastable state pair. The A_{ij} values for the two radiative decays are displayed in Table 1 and added to the $R_{2 \to 1}$ coefficient for the 247.9 nm line and $R_{3 \to 2}$ for the 940.6 nm line. Solving the system of equations in the CRM generates the fractional level populations for each of the four levels.

B. Model Application

Electron temperature and density profiles used for correcting measured emission data were generated with the Hall2De code, a two-dimensional, axisymmetric computation solver of the conservation equations that govern the evolution of the partially ionized gas in Hall thrusters. Hall2De, its governing equations, methodology, and benchmarking are described elsewhere.[19–21] Numerical data used in this work was generated for the work described in Kamhawi;[22] specific details of the modeling configuration are detailed there. The electron temperature and density profiles used in the CRM are shown in Fig. 3.

Modelling performed by Choi[23] found that carbon density in front of the IFPC is dominated by carbon sputtered from the IFPC. The contribution to the carbon density from the outer front pole cover (OFPC) and facility backsputter in the region in front of the IFPC are an order of magnitude or more lower than the IFPC contribution. The OES probe collected line integrated emission throughout its collection cone. Volumes in the collection cone downstream of the IFPC have significantly less carbon density than in front of the IFPC, particularly in the region downstream of the discharge channel; carbon line emission recorded by the OES should be dominated by carbon sputtered from the IFPC.

Following from Eq. (1), the emission intensity is directly proportional to the population of the upper state of the transition (N_j). The CRM approximates the set of rate equations (Eq. (3)), relating electron density, initial state populations, and rate coefficients to the resultant state populations. The model is steady state; the initial populations are the same as the final ones. The output is the relative populations of the states in the model, dependent on electron temperature and density. Normalizing the OES signal by the electron density relative to a reference point results in an estimate of the carbon population in the upper state of the 247.9 nm transition relative to that same point. Since the carbon density in front of the IFPC is predominantly the result of the sputtered carbon from the IFPC, this signal should be proportional to the

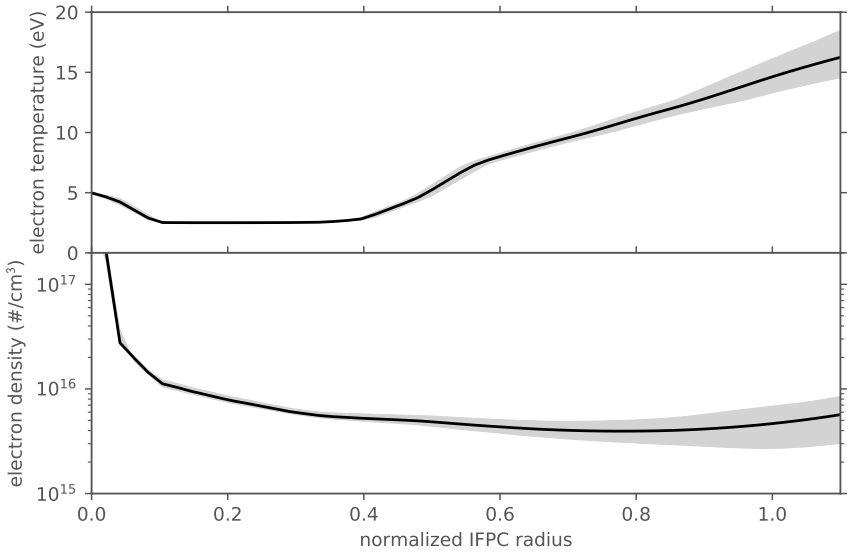

Figure 3: Representative electron temperature and density profiles extracted from Hall2De modeling. Shown are profiles from the B2 configuration. The solid lines depict the mean values for T_e and n_e in a 5 mm span in front of the IFPC, while the shaded regions represent the range of T_e and n_e in the same region.

measured erosion rate. The emitted signal is also normalized to the same reference point. Thus, $\Delta n_C(r)$, the measure of carbon density as a function of radius, relative to a point r_0 on the IFPC is

$$\Delta n_C(r) = \frac{n_C(r)}{n_C(r_0)} \propto \frac{I_{247.9}(r)}{I_{247.9}(r_0)} \frac{n_e(r)}{n_e(r_0)} C_{\text{crm}}(r) \tag{12}$$

where r_0 is the reference radius and C_{crm} is CRM correction factor.

For a given T_e and n_e, the relative population of the upper state of the 247.9 nm line can then be calculated with the CRM. The correction factor calculated with the CRM model along the radius of the IFPC is displayed in Fig. 4; it is dependent on both electron temperature and density. The electron density normalization factor is also shown in this figure. The reference point r_0 for normalization is just inboard of the outer edge of the IFPC at $r \sim 0.90$.

III. Test Configuration

A series of magnetic field optimization tests were performed on the TDU-1 thruster. The objective was to evaluate several candidate magnetic field topologies and find a balance between discharge channel erosion and front pole erosion, while maintaining performance and stability during thruster operation. Three candidate magnetic field topologies (B1, B2 and B4) were designed, modeled, and tested. Testing of the candidate magnetic field topologies was performed at the NASA GRC Vacuum Facility 6 (VF-6) in two phases. During Phase I, LIF measurements were performed on the baseline (B0) and candidate magnetic field topologies (B1, B2, and B4).[22] In Phase II, the performance, stability, wear (except for B4), plasma plume, and optical emission spectroscopy measurements were performed to provide data to assess the optimal configuration. Multiple firing conditions were characterized for each magnetic configuration. Following characterization, short duration wear tests of 250 h were completed in the 600 V, 21 A firing condition. The thruster's magnetic topology was then reconfigured and the IFPC erosion was measured using a chromatic, white light, non-contact profilometer before undertaking the next step in the test sequence. Additional details of the magnetic field topology optimization motivation, design, modeling, and testing can be found in Kamhawi.[11,22]

A. Technology Demonstration Unit

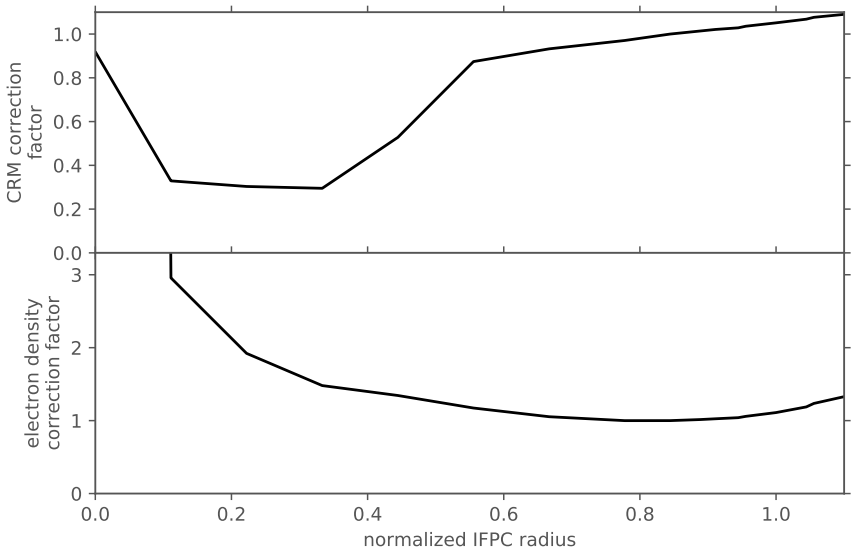

Figure 4: Correction factors for observed emission intensities resulting from changes in T_e and n_e.

The design of HERMeS TDU-1 incorporates technologies developed by NASA over nearly two decades. The thruster incorporates a magnetic shielding topology to eliminate discharge channel erosion as a life limiting mechanism.[24,25] The result is a significant increase in the operational lifetime, with HERMeS being designed to operate at 3,000 sec specific impulse and a projected life of >50 kh. The TDU-1 thruster shares key design features with the other TDU thrusters which include magnetic field topology, propellant manifold design, and discharge channel dimensions.

B. Space Simulation Facility

Testing of the HERMeS TDU-1 thruster was performed in VF-6 at NASA GRC.[26,27] The VF-6 main chamber is 7.6 m in diameter, 21 m long, and is evacuated with 12 internal nude cryo pumps. For the test campaign discussed in this paper, the TDU-1 Hall thruster was located in the main volume of the chamber. Facility pressure was monitored with two xenon calibrated Stabil ion gauges. The power supplies, data acquisition, and propellant flow system have been previously used and are described in detail in Peterson.[27]

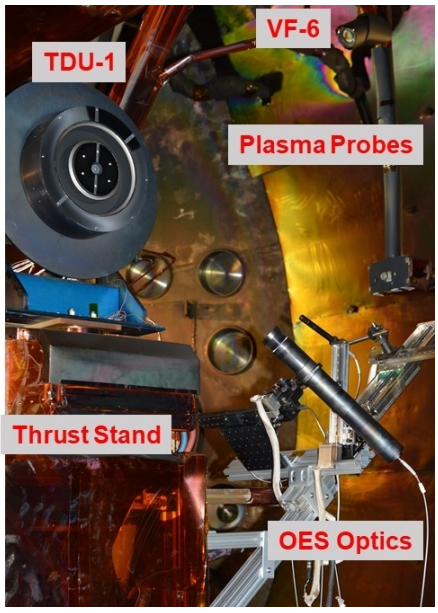

Figure 5: OES probe setup.

C. Optical Emission Spectroscopy Configuration

The OES diagnostic system utilized for the erosion measurements consisted of a UV-visible spectrometer, an optical probe, and connecting fibers. The optical probe incorporated UV-silica lenses, flat windows, optical tubes, and SMA fiber optic connectors. The optical probe used 5 cm diameter lenses matching the acceptance angle of the 400 µm diameter UV-VIS fiber optic cables. The optical probe was mounted on a translation stage with a range of motion of 200 mm. The probe was mounted approximately 0.5 m away from the axis of the thruster and approximately 0.5 m in front of the front plane of the thruster. The probes were downstream of the thruster exit plane to both allow a small collection volume at the thruster surface and to keep the probes collection volumes downstream of the primary ionization and acceleration zones in the channel. The optical probe was aligned with a laser before pump down of the vacuum facility. A picture of the setup can be seen in Fig. 5.

The spectrometer used had a measurement range of 224–450 nm. Wavelengths were calibrated with an Hg/Ne light source. Dark spectra were captured before each session. All captured spectra used an 8 s integration time and averaged 4 individual captures. A scan of 10 points took approximately 5 min to complete.

The optical probe was capable of scanning vertically across the TDU thruster face, ranging from the outer wall of the discharge channel to the center mounted cathode. Most data was captured at 9 points on the IFPC, with 8 of them being on the outer half of the IFPC and one at the inner third.

D. Inner Front Pole Cover Configuration

Graphite masks were installed on the IFPC to provide unexposed surfaces for use as a reference for post-test analysis with the non-contact profilometer. The graphite surface of the IFPC was polished prior to installation in order to minimize the variation in pre-test surface roughness and thus provide as uniform a baseline surface as possible. Unlike in previous wear tests, the IFPC was re-polished prior to each segment of the magnetic configuration optimization test.[9] Two 0.5-mm thick graphite masks were installed at the 12 oclock and 6 oclock locations of the IFPC. These masks are identical to the graphite masks used during previous TDU wear tests.[9]

IV. Results and Discussion

The wear test results found that inner front pole cover erosion rates of configurations B1 and B2 were on average 35% and 65%, respectively, lower than that of the baseline configuration B0. The truncation of the wear test data near the inner IFPC edge is due to the fact that the employed masks only covered approximately 95% of the IFPC. Near the center of the IFPC, the mask fastener interfered with the unexposed reference surface, thus precluding data analysis in this region. The results of the erosion measurements are summarized in Fig. 6 and a more detailed description and analysis can be found in Kamhawi.[11]

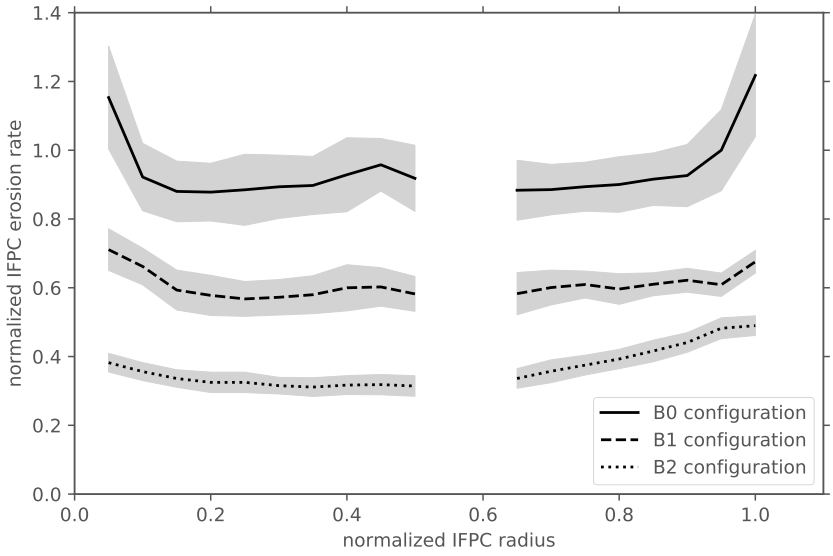

Figure 6: Erosion rates measured after the short duration wear test in each magnetic configuration, as measured by the chromatic, white light non-contact profilometer. Erosion rates were not measured in the center of the IFPC as the mask fastener interfered with the unexposed reference surface.

For the OES erosion measurements, it was required to normalize each data set to the erosion measured with the non-contact profilometer. This is the result of changes in the OES setup between magnetic configurations, preventing the direct comparison of OES data from different configurations.

Figure 7a compares the compensated and uncorrected OES signal captured during 5 min of thruster operation to the erosion measured with the non-contact profilometer after the 250 h wear test. The compensated

OES signal agrees well with the erosion profile measured with the profilometer. From Fig. 4, it can be seen that both the CRM correction factor and the density normalization are relatively smoothly varying and small in magnitude in the range of $r = 0.5$–1.0, leading to only a small overall compensation of the raw OES signal; little correction is needed for the OES signal in this region. The point at $r \approx 0.33$ appears to be over corrected by the model. This will be discussed later. The B1 configuration exhibits similar trends, as can be seen in Fig. 7b. In Figs. 7 to 10, all erosion is normalized to the erosion rate as measured by the profilometer at $r \sim 0.90$.

Figure 8 shows data from two different OES scans of the B2 configuration. The first scan in Fig. 8a is a short scan similar to the B0 and B1 scans, and shows very similar behavior: good agreement with the profilometer erosion profile from $r = 0.5$–1.0, and over correction of the $r \approx 0.33$ data point. A second OES scan with more data points across the inner IFPC is displayed in Fig. 8b. The OES trend is more illuminating here in the range of $r = 0.1$–0.6. The uncorrected signal shows a gentle increase moving inboard on the IFPC. The compensated signal is erratic, with some points being close to the profilometer measured rate, and some being higher or lower. The compensated OES point at $r \approx 0.3$ is similar to the short scans for the B0, B1, and B2 configurations. Inspecting the electron density and the CRM correction factor provides some insight.

While the density does continue to vary smoothly moving inward from $r = 0.5$ on the IFPC, the CRM correction factor rapidly drops. As can be seen from the CRM correction factor in Fig. 4, the factor drops to a low value in the range $r = 0.1$–0.35. Plotting the CRM correction factor as a function of T_e for a nominal electron density (see Fig. 9), it is readily apparent that the CRM correction factor is very sensitive to T_e in the range of $T_e = 1.5$–$3.5\,\mathrm{eV}$, with maximum sensitivity occurring at $T_e \sim 2.4\,\mathrm{eV}$, depending on the specific value of n_e. The electron temperature in the range $r = 0.1$–0.35 from the Hall2De simulation is $T_e \sim 2.5\,\mathrm{eV}$; essentially directly in the region of maximum sensitivity. As a result, the likelihood for error in the CRM correction factor in this radial range is high due to its sensitivity to input parameters. Physically, this is sensible. The upper state in the 247.9 nm transition has an energy of $E_j = 7.68\,\mathrm{eV}$ and $E_i = 2.68\,\mathrm{eV}$ for the lower state. Collisional excitation to the upper state rapidly increases in this range before beginning to roll off. Additionally, excitation into the upper state is significantly reduced when the local electron temperature is lower than roughly half of the energy of the upper state. It should be noted that the absolute magnitude of the raw OES signal in the region was sufficient and not subject to a poor signal-to-noise ratio.

In order to get an idea of the actual sensitivity of the CRM in this region of the IFPC (and range of T_e), the electron temperature profile used for the CRM calculation was adjusted until the compensated OES signal was in agreement with the erosion profile measured by the profilometer. This new electron temperature profile and compensated OES signal are displayed in Fig. 10. The more linear nature of the adjusted electron temperature profile is more in agreement with the temperature profile measured in the prior tests, where the steep drop in temperature near $r \approx 0.5$ was not observed.[14] The necessary adjustment in electron temperature was $0.3 < \Delta T_e < 1.25$, with an average of $0.75\,\mathrm{eV}$. In addition to the 'adjusted' CRM compensated OES signal, the input electron temperatures were varied about the adjusted point in a range of $\pm 1\,\mathrm{eV}$. This range is represented by the error bars in the compensated OES signal in Fig. 10. Clearly, the model is very sensitive where the electron temperature is low and relatively small changes or errors in the T_e profile used can have a large impact. Once $T_e \gtrsim 6\,\mathrm{eV}$, the CRM correction factor changes less than 10 % per eV, a value which continues to decrease as the electron temperature increases. This can be seen in the very small span of the error bars on the compensated OES signal for $r > 0.5$ in Fig. 10.

For some of the tested magnetic field configurations, OES data was acquired during scans of the magnetic field strength. Though Hall2De derived profiles for n_e and T_e were not available, it is still instructive to to inspect the resulting trends. The magnetic field was scanned from 0.75–1.25 of the nominal magnetic field strength B_{nom}. Representative results from the magnetic field scan of the B0 configuration are shown in Fig. 11. Temperature and density profiles for the nominal magnetic field B_{nom} modeling results were used to compensate the recorded OES signal for the off-nominal B strengths. Only the outer half of the IFPC is shown to minimize the impact of the T_e sensitivity previously discussed. It is evident that that as the magnetic field strength is increased, OES signal also increases. Assuming n_e is the same for different field strengths, this increase in signal implies that erosion rates have also increased. However, this assumption can not necessarily be made; it is possible that electron density increases in front of the IFPC as a result of a stronger magnetic field, accounting fully for the observed increase in OES signal. It is more likely that that if there is an increase in n_e with increasing magnetic field, it contributes only a portion of the increase in observed OES signal. As a result, it is likely that at least some of the observed increased emission is due to an

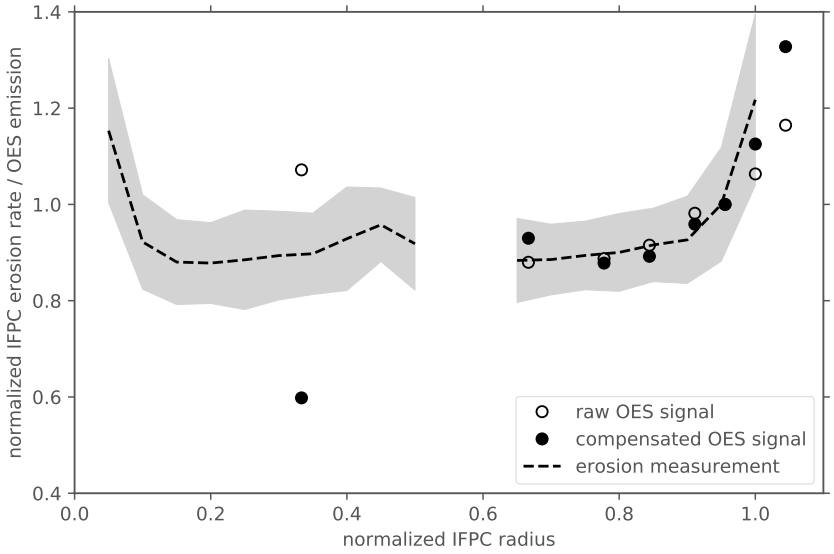

(a) B0 configuration

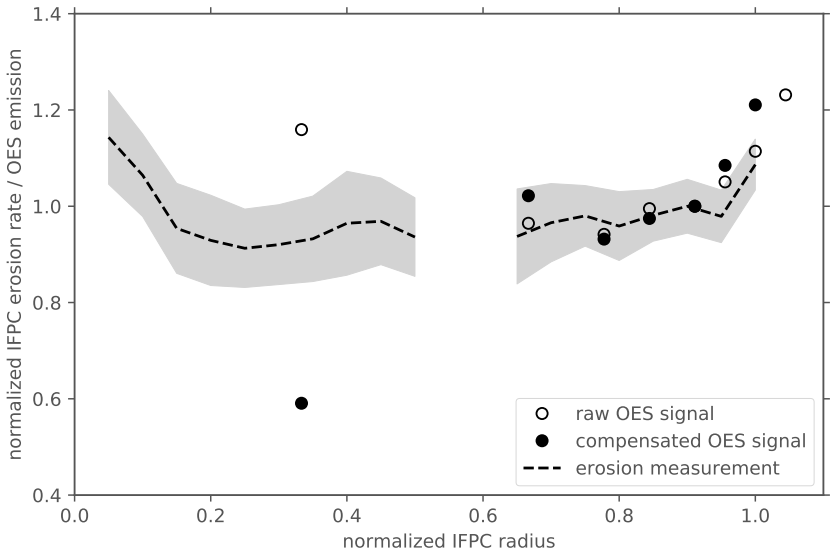

(b) B1 configuration

Figure 7: Erosion and OES signal measured from B0 and B1 configurations. Error in the erosion measurement is represented by the gray band. Raw and CRM/density compensated OES signal are plotted.

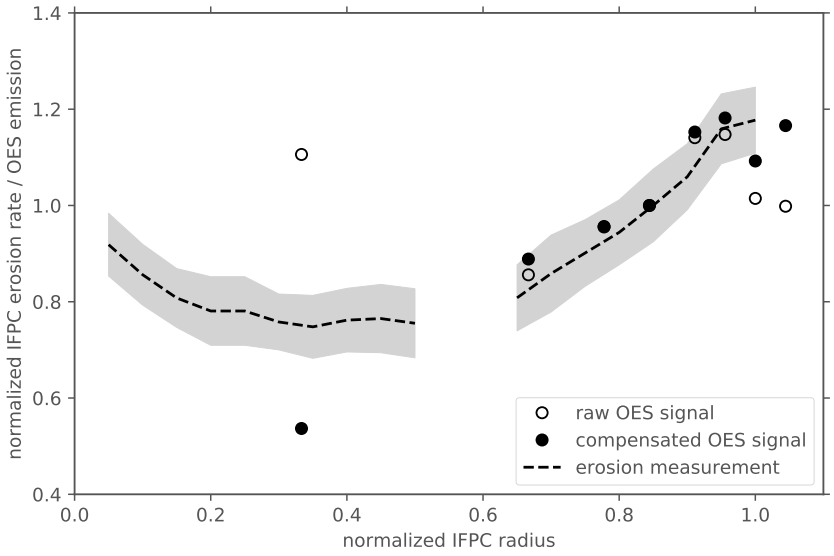

(a) B2 configuration

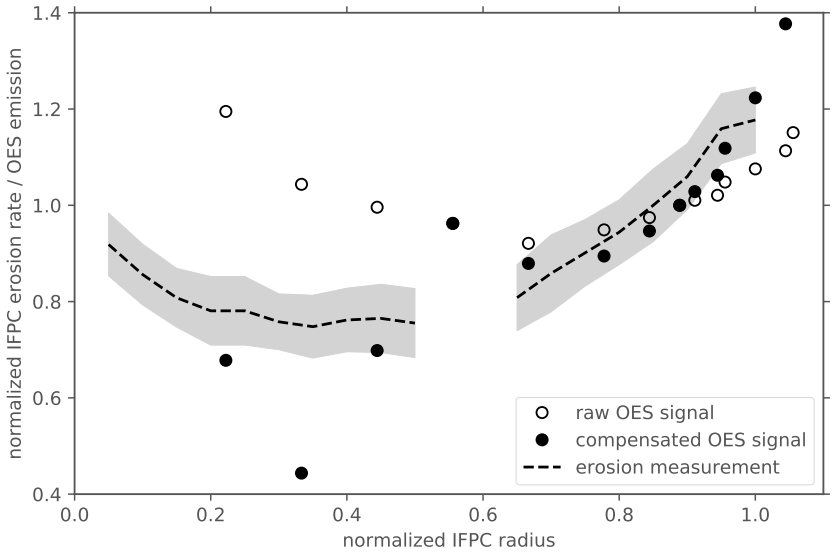

(b) B2 configuration full scan

Figure 8: Erosion and OES signal measured from two measurements of the B2 configuration. Error in the erosion measurement is represented by the gray band. Raw and CRM/density compensated OES signal are plotted.

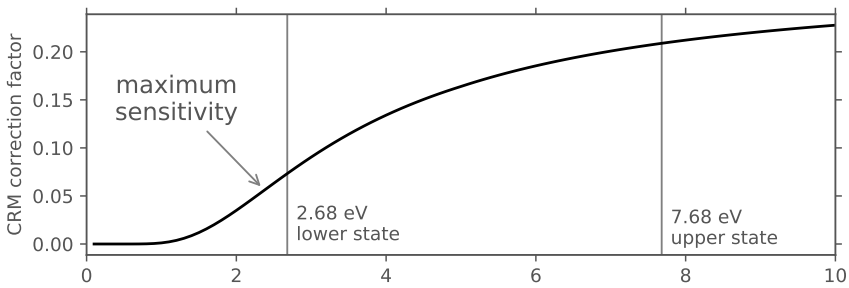

Figure 9: CRM correction factor as a function of electron temperature for a fixed electron density. The maximum rate of change in the factor occurs at low energies near the lower energy state of the 247.9 nm transition.

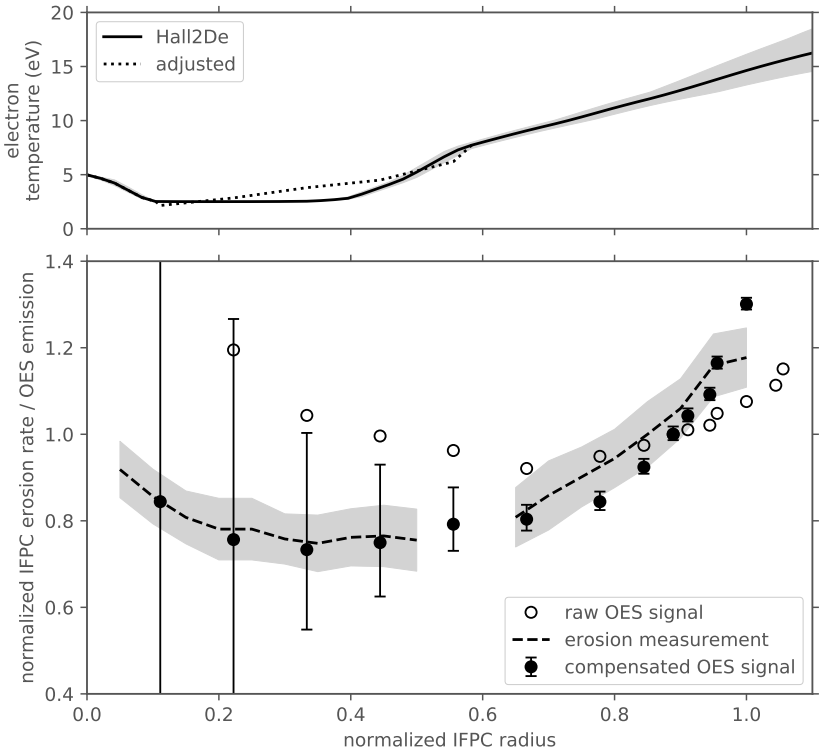

Figure 10: (upper) Simulated electron temperature and adjusted electron temperature. (lower) Erosion and OES signal measured from the B2 configuration (same as Fig. 8b). Error in the erosion measurement is represented by the gray band. Raw and CRM/density compensated OES signal are plotted. The compensated OES signal uses the adjusted electron temperature from the upper plot instead of the values from Hall2De modeling. The error bars for the compensated OES signal represent the variation in the compensated OES signal due to a ± 1 eV variation in the input electron temperature.

increase in carbon sputtering with increasing magnetic field. This is in agreement with the trends observed in previous tests with a discharge voltage of 300 V.[9] The increase in OES signal for several configurations is mostly linear and has a mean value of approximately 3.0–3.5% per 10% increase in magnetic field strength.

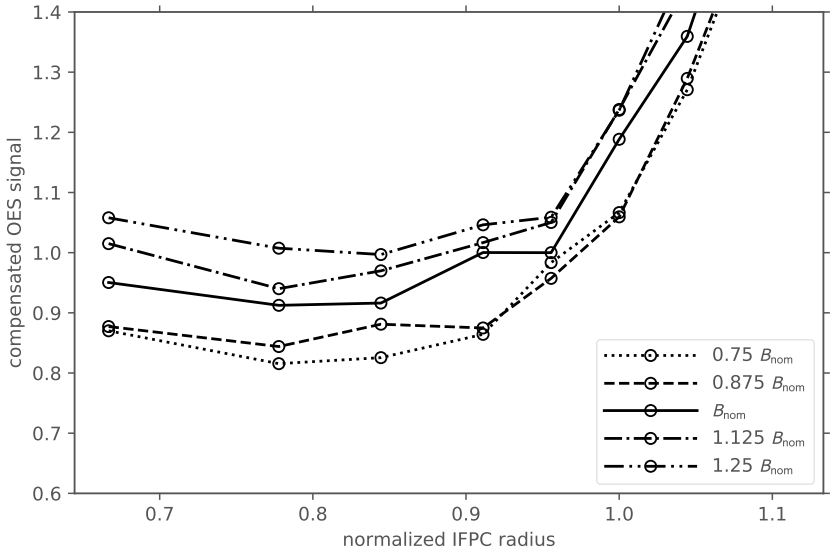

Figure 11: Compensated OES signal measured for a magnetic field scan in the B0 configuration.

V. Future Work

A more detailed CRM is probably warranted for describing the level populations available to the sputtered carbon atoms. The presented model does not attempt to account for many available states for carbon, nor does it account for the effect of ionization. At the same time, the very presence of strong emission at 247.9 nm is evidence that the sputtered carbon is not fully ionized and that a significant population of carbon atoms exist in the relevant states. It has also been shown that in the hotter part of the ambient plasma corresponding to r =0.5–1.0, electron density is the primary quantity which must be accounted for in order to correlate raw OES signal to carbon density. Regardless, a more detailed model would more accurately calculate population densities. Furthermore, additional emission lines could be monitored if sufficiently strong and represented in the model, which could help refine local electron temperature and density. The line at 940.6 nm might be a good candidate for this.

Additionally, measurements of local electron density and temperature would also refine the output of the OES erosion measurement. In addition to electrostatic probing, non-intrusive optical emission spectroscopy techniques exist for characterizing these two quantities, and if implemented in a rigorous fashion, could provide the necessary inputs to the CRM to provide proper interpretation of the OES data without needing sophisticated modeling.

VI. Conclusion

Optical emission spectroscopy has been used to measure relative erosion rates on the inner front pole cover of the HERMeS TDU-1 thruster during a magnetic configuration optimization test campaign. The diagnostic shows promise for in-situ measurement of carbon erosion from plasma facing components on Hall thrusters. Good correlation exists between the compensated OES signal and erosion profiles measured after 250 h duration wear tests for the 3 tested magnetic configurations, particularly in the region of higher electron temperatures where the collisional-radiative model is less sensitive to changes in electron temperature. Accurate electron density and temperatures profiles are needed to properly interpret the raw OES signals and correlate the results to erosion of the front pole covers of the Hall thruster.

Acknowledgments

The authors thank the Space Technology Mission Directorate through the Solar Electric Propulsion Technology Demonstration Mission Project for the joint NASA GRC and JPL development of the Advanced Electric Propulsion System. The authors thank Todd Tofil for managing the electric propulsion work within the SEP Project and Richard Hofer for leading the AEPS thruster development effort. The authors also thank the Michael Mcvetta and technicians of the Space Facilities Branch at NASA GRC who enabled all of the test results presented herein.

References

[1]Congress, "National Aeronautics and Space Administration Transition Authorization Act of 2017," 2017.

[2]Gerstenmaier, W., "Progress in Defining the Deep Space Gateway and Transport Plan," 2017, NASA Advisory Council Human Exploration and Operations Committee Meeting, Washington, DC.

[3]NASA, "NASA Awards Artemis Contract for Lunar Gateway Power, Propulsion," `https://www.nasa.gov/press-release/nasa-awards-artemis-contract-for-lunar-gateway-power-propulsion`, 2019.

[4]Ticker, R., Gates, M., Manzella, D., Biaggi-Labiosa, A., and Lee, T., "The Gateway Power and Propulsion Element: Setting the Foundation for Exploration and Commerce," *2019 Joint Propulsion Conference*, Indianapolis, IN, United States, 2019.

[5]Smith, B. K. N., "Solar Electric Propulsion Vehicle Demonstration to Support Future Space Exploration Missions," *Space Propulsion 2012*, Bordeaux, France, May 2012.

[6]Hofer, R. R., Goebel, D. M., Mikellides, I. G., and Katz, I., "Magnetic Shielding of a Laboratory Hall Thruster. II. Experiments," *Journal of Applied Physics*, Vol. 115, No. 4, Jan. 2014.

[7]Kamhawi, H., "Performance and Thermal Characterization of the NASA-300MS 20 kW Hall Effect Thruster," *33rd International Electric Propulsion Conference*, Washington, DC, United States, Oct. 2013.

[8]Shastry, R., "Near-Surface Plasma Characterization of the 12.5-kW NASA TDU1 Hall Thruster," *51st AIAA/SAE/ASEE Joint Propulsion Conference*, Orlando, FL, United States, July 2015.

[9]Frieman, J. D., Kamhawi, H., Williams, G., Herman, D., Peterson, P. Y., Gilland, J. H., and Hofer, R., "Long Duration Wear Test of the NASA HERMeS Hall Thruster," *54th AIAA/SAE/ASEE Joint Propulsion Conference*, Cincinnati, OH, United States, 2018.

[10]Frieman, J. D., Kamhawi, H., Williams, G., Huang, W., Herman, D., Peterson, P., and Gilland, J. H., "Completion of the Long Duration Wear Test of the NASA HERMeS Hall Thruster," *2019 Joint Propulsion Conference*, Indianapolis, IN, United States, 2019.

[11]Kamhawi, H., "Performance, Plume, Stability,and Wear Characterization of Three Alternate Magnetic Field Topologies in the Hall Effect Rocket with Magnetic Shielding," *36th International Electric Propulsion Conference*, Vienna, Austria, 2019.

[12]Williams, G. J., "Wear Testing of the HERMeS Thruster," *52nd AIAA/SAE/ASEE Joint Propulsion Conference*, Salt Lake City, UT, United States, July 2016.

[13]Williams, G. J., "Optical Characterization of Component Wear and Near-Field Plasma of the Hermes Thruster," *62nd Joint Army-Navy-NASA-Air Force Meeting*, Nashville, TN, United States, June 2015.

[14]Williams, G., Choi, M., Kamhawi, H., Huang, W., Herman, D., Gilland, J., and Urban, P., "Assessment of HERMeS Wear Trends via Optical Emission Spectroscopy," *65th Joint Army-Navy-NASA-Air Force Propulsion Meeting*, 2018.

[15]Rock, B. A. M., "Rapid Evaluation of Ion Thruster Lifetime Using Optical Emission Spectroscopy," *18th Intern. Elec. Propulsion Conf.*, Alexandria, VA, United States, Jan. 1985.

[16]Kramida, A., Ralchenko, Y., Reader, J., and NIST ASD Team, "NIST Atomic Spectra Database," `https://physics.nist.gov/asd`, 2018, National Institute of Standards and Technology, Gaithersburg, MD.

[17]Sobel'man, I. I., Vainshtein, L., and Yukov, E. A., *Excitation of Atoms and Broadening of Spectral Lines*, Springer Series on Atomic, Optical, and Plasma Physics, Springer-Verlag, Berlin Heidelberg, 2nd ed., 1995.

[18]Chernyi, G. G., Losev, S. A., Macheret, S. O., and Potapkin, B. V., editors, *Physical and Chemical Processes in Gas Dynamics: Physical and Chemical Kinetics and Thermodynamics of Gases and Plasmas, Volume II*, American Institute of Aeronautics and Astronautics, Reston ,VA, Jan. 2004.

[19]Mikellides, I. G. and Katz, I., "Numerical Simulations of Hall-Effect Plasma Accelerators on a Magnetic-Field-Aligned Mesh," *Physical Review E*, Vol. 86, No. 4, Oct. 2012.

[20]Katz, I. and Mikellides, I. G., "Neutral Gas Free Molecular Flow Algorithm Including Ionization and Walls for Use in Plasma Simulations," *Journal of Computational Physics*, Vol. 230, No. 4, Feb. 2011.

[21]Lopez Ortega, A. and Mikellides, I. G., "A New Cell-Centered Implicit Numerical Scheme for Ions in the 2-D Axisymmetric Code Hall2De," *50th AIAA/ASME/SAE/ASEE Joint Propulsion Conference*, American Institute of Aeronautics and Astronautics, Cleveland, OH, July 2014.

[22]Kamhawi, H., Huang, W., and Mikellides, I., "Optimization of the Magnetic Field Topology in the Hall Effect Rocket with Magnetic Shielding," *54th AIAA/SAE/ASEE Joint Propulsion Conference*, Cincinnati, OH, United States, July 2018.

[23]Choi, M., Yim, J., Williams, G., Herman, D., and Gilland, J. H., "Hybrid-PIC Simulation of Backsputtered Carbon Transport in the Near-Field Plume of a Hall Thruster," *35th International Electric Propulsion Conference*, Atlanta, GA, United States, 2017.

[24]Hofer, R., Kamhawi, H., Herman, D., Polk, J., Snyder, J. S., Mikellides, I., Huang, W., Myers, J., Yim, J., Williams, G., et al., "Development Approach and Status of the 12.5 kW HERMeS Hall Thruster for the Solar Electric Propulsion Technology Demonstration Mission," *30th International Electric Propulsion Conference*, Kobe, Hyogo, Japan, 2015.

[25]Mikellides, I. G., Hofer, R. R., Katz, I., and Goebel, D. M., "Magnetic Shielding of Hall Thrusters at High Discharge Voltages," Vol. 116, No. 5, 2014.

[26]Patterson, M. J. and Sovey, J. S., "History of Electric Propulsion at NASA Glenn Research Center: 1956 to Present," *Journal of Aerospace Engineering*, Vol. 26, No. 2, April 2013.

[27]Peterson, P. Y., Huang, W., Yim, J., Haag, T., Mackey, J., McVetta, M., Sorrelle, L., Tomsik, T., Gilligan, R., and Herman, D., "Reconfiguration of NASA GRC's Vacuum Facility 6 for Testing of Advanced Electric Propulsion System (AEPS) Hardware," *35th International Electric Propulsion Conference*, Atlanta, GA, United States, 2018.